Poly(ether imide) Alumina Nanocomposites: Interphase Properties Determined from Free Volume Element Radius Distributions

Junkun Pan, Aaron P. Charnay, and Michael D. Fayer*

Cite This: https://doi.org/10.1021/acs.macromol.4c00868

Read Online

ACCESS | Metrics & More | Article Recommendations | Supporting Information

ABSTRACT: Ultrafast infrared (IR) spectroscopy was used to characterize the free volume element (FVE) radius probability distributions (RPDs) of poly(ether imide) (PEI) alumina nanocomposites. The nanocomposites (0−2 wt %) were prepared with 20 nm diameter spherical Al_2O_3 nanofillers and a small amount of phenyl selenocyanate (PhSeCN) as IR vibrational probes. Restricted orientation anisotropy method (ROAM), an ultrafast IR technique, was used to measure FVE radii. The results yield RPDs as a function of the nanoparticle concentration. The RPDs were decomposed into bulk PEI and interphase region contributions. The ROAM results demonstrate that the polymer chain packing in PEI nanocomposites is significantly altered from that of pure PEI. The average FVE radius increases with increasing nanofiller content. The RPDs indicate that subensembles with smaller radii are disproportionately affected by the presence of the Al_2O_3 nanofillers, causing the width of the distribution to narrow. The FVE RPDs for the interface regions reveal a distribution with an average radius ∼0.2 Å larger but significantly narrower than the pure PEI distribution. Finally, the interface volume fraction for each nanocomposite sample was determined from the differences in the RPD curves, and the effective interfacial layer thickness was found to be 19.2 ± 0.5 nm. The results demonstrated that FVE characteristics are strongly affected by the proximity to nanoparticles. The nature of the FVEs in the interfacial regions provides information about the microscopic origin of the polymer nanocomposite material's properties.
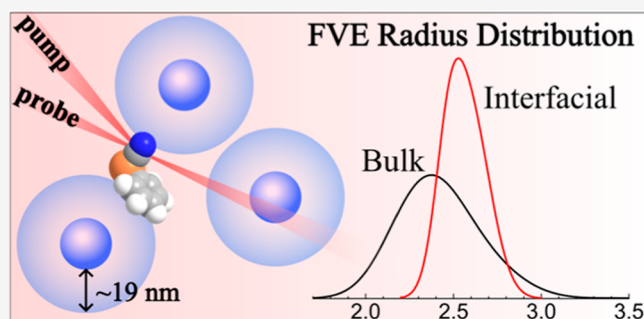
1. INTRODUCTION

Since the discovery that adding nanoscale Montmorillonite clay to nylon-6 significantly improves its bending modulus and heat resistance,[1] polymer nanocomposites (PNCs) have gained increasing attention, with applications ranging from glucose biosensors[2] and gas separation membranes[3,4] to dielectric materials.[5−10] PNCs are made by incorporating small amounts, usually <1−5%, of nanoscale fillers, which have at least one dimension below 100 nm.[11] Nanofillers vary in both composition and morphology. Nanofiller types include zero-dimensional spherical metal/metal oxide nanoparticles,[6,8,9,12−15] one-dimensional materials like carbon nanotubes,[16,17] and two-dimensional nanoclays.[18]

Unlike most traditional polymer composites, PNCs only require a small volume fraction of the nanofiller to cause significant bulk property changes. For example, Zhang and co-workers demonstrated that by incorporating only 0.32 vol % low-dielectric-constant inorganic filler alumina (Al_2O_3), the dielectric constant of poly(ether imide) (PEI) was improved by 55% over that of the pure polymer.[10] Similar trends have also been observed in other PNC systems.[16,17,19] This dramatic improvement in properties is generally not explained by simple mixing rules. Instead, it has been attributed to the interactions between the inorganic nanofiller and the polymer matrix, which creates an interfacial layer (interphase). The interphase

has properties distinct from the bulk.[20,21] Multiple models have been proposed to describe the characteristics of the interface, such as the intensity model proposed by Lewis,[20,22] the multilayered core model by Tanaka et al.,[23] the interface volume model by Raetzke and Kindersberger,[24,25] and the chain alignment model by Andritsch et al.[26] Lewis proposed that the nanoparticle core is positively charged, which will produce an electrical double layer (Stern/Gouy−Chapman layer) that diffuses outward.[20,22,27] Tanaka built upon this model and described three layers surrounding the nanoparticle core.[23] The first layer is called the bonded layer, where the polymer tightly adheres to the nanoparticle surface; the second layer, the bound layer, is a polymer layer that has a strong interaction with the first layer; and the third layer is the loose layer, which is loosely coupled to the second layer. Additionally, the electrical double layer described by Lewis overlaps these three layers. The interface volume model[25] adopted the

multilayered core model[23] and systematically calculated the volume fraction of the nanocomposite interfacial area for spherical nanofillers, assuming uniform dispersion and particle diameters. For example, a nanocomposite with 2 vol % nanofiller with 30 nm diameter particles would have an interphase volume fraction of more than 30%, assuming an interfacial layer thickness of 5 nm. Since the interphase occupies such a large volume fraction of the nanocomposite material, understanding the microscopic characteristics of the interfacial area could significantly accelerate the practical applications of the PNCs.

Many experimental methods have been used to characterize the thickness and physical properties of the interphase. Articles by Cheng et al.[28] and Wang et al.[29] provide comprehensive overviews of these techniques. Methods include small angle X-ray/neutron scattering (SAXS/SANS),[30−32] broadband dielectric spectroscopy (BDS),[33−35] atomic force microscopy (AFM),[36−39] and positron annihilation lifetime spectroscopy (PALS).[40−42] Despite the large number of studies dedicated to characterizing the properties and the thicknesses of interphases, there are significant inconsistencies among the length scales extracted from different methods, ranging from 1 nm to more than 100 nm.[32,33,43]

Recently, a new technique, the restricted orientation anisotropy method (ROAM), based on ultrafast infrared (IR) spectroscopy, was developed for measuring the free volume element (FVE) radii and radius probability distributions (RPDs) in polymeric materials.[44−46] the ROAM combines the measurements of the orientational relaxation of the vibrational probe molecules embedded in the FVEs with the physical dimensions of the probe as a "molecular ruler" to extract the radii of the FVEs. Previously, the ROAM was successfully applied to characterize a variety of pure polymer systems.[44−46] The ROAM experiments show high sensitivity to different polymer environments and the modification of polymer end groups.[46,47] The ROAM technique was refined recently, and definitive tests were performed.[44] Six vibrational probes with different shapes and lengths were used to perform ROAM measurements on amorphous polystyrene (PS). The measurements yielded the same FVE radius within a few hundredths of an Å for each of the six probes, demonstrating the method's accuracy.[44] It is worth noting that the average FVE radius in the PS study agreed with two separate PALS measurements.[44,48,49] In addition to demonstrating the ROAM's accuracy, the studies eliminate the possibility that a small amount of embedded vibrational probe molecules influence the FVE sizes.

In the present paper, we expand the application of the ROAM to PNC systems by characterizing the FVEs of poly(ether imide) alumina nanocomposites (PANCs). Samples were made with PEI as the polymer matrix and 0.5, 1, or 2 wt % 20 nm diameter spherical γ-Al_2O_3 nanoparticles as the nanofillers. The ROAM measurements demonstrated that adding 20 nm alumina nanoparticles to the PEI matrix significantly altered the polymer chain packing. The average FVE radius increased in the interfacial layers with increasing nanofiller fraction. Subensembles of FVEs with smaller radii were shown to be affected more by the addition of nanofillers than the larger FVEs. The distribution of FVE radii in the interfacial layer was determined from the changes in the RPD curves. The FVEs in the interfacial layer have larger average radii and narrower distributions than bulk PEI. Finally, the interphase volume fraction for each nanocomposite was

calculated to extract the effective interfacial layer thickness. Using the interface volume model,[50] the layer thickness was determined to be 19.2 ± 0.5 nm. The measured properties provide a wealth of information regarding the microscopic structural change in the interfacial layer, which may facilitate the development of future PNCs.

2. EXPERIMENTAL METHODS

2.1. Sample Preparation. PEI (melt index 9 g/10 min), 1-methyl-2-pyrrolidinone (NMP), and phenyl selenocyanate (PhSeCN) were purchased from Sigma-Aldrich. 20 wt % aluminum oxide nanoparticle dispersion in NMP was purchased from US-Nano. The average diameter of the nanoparticles was 20 nm, as specified by the supplier. All chemicals were used without further purification. PEI and its nanocomposite films with weight fractions of 0.5, 1, and 2% alumina nanoparticles (designated as PANC-0.5, PANC-1, and PANC-2, respectively) were prepared using solvent casting. The required amounts of aluminum oxide nanoparticle suspension and PEI pellets were measured and dissolved in NMP to form suspensions with a 0.5 g/mL polymer concentration. To ensure the nanoparticles were well dispersed, the suspension was subjected to high-power probe sonication at 360 W for 30 min using a 1 s on/1 s off sequence. Immediately after the sonication step, 3 mL of the uniform dispersion was cast onto a 2-in diameter leveled glass substrate and heated to 85 °C overnight to solidify the film. Then, the polymer films were peeled from the substrate and dried in a vacuum oven at 120 °C for 24 h to remove the solvent.

The films were then soaked in 2 vol % PhSeCN solution in methanol for 48 h. This step has two purposes: diffusing the vibrational probes into the polymer FVEs and solvent exchange with methanol to remove residual NMP solvent. Finally, the soaked films were dried in a vacuum oven at 140 °C for 48 h and at 160 °C for 24 h to remove methanol and NMP solvent. The resulting sample films have thicknesses of 60 ± 10 μm. Notably, a fraction of the PhSeCN probe molecules diffuse out of the film during the heat treatment process. The heat treatment at 160 °C was extended to 48 h, which lowered the probe content by approximately 50% to ensure that the probe content was low enough. The sample with the lower probe concentration yielded the same anisotropy decay curves, which confirmed that adding vibrational probes at sufficiently low concentrations did not alter the results. The vibrational probe and residual solvent contents of all films were characterized by NMR as described below. Additionally, the nanoparticle dispersion states were characterized by scanning electron microscopy (SEM) as presented below.

For ultrafast IR measurements, four small pieces are cut from each film and stacked to increase the optical path length. Index-matching oil between the films reduced surface reflections and light scattering. The stacked films were sealed in sample cells with two CaF_2 windows separated by a 250 μm Teflon spacer.

2.2. NMR Characterization. ^{1}H NMR was used to quantify the films' residual solvent content and vibrational probe (PhSeCN) content. 10 mg of the sample was cut from each film and dissolved in 750 μL of deuterated dichloromethane. The spectra were collected in a 400 MHz Varian NMR spectrometer using the VNMRJ 4.2 software. The NMP peaks were integrated and compared to a characteristic PEI monomer peak. The NMR measurements confirm that the final films used for measurements had less than 1 wt % residual NMP solvent and less than 2 wt % PhSeCN probes. The complete details of the characterization and NMR spectra of the samples are presented in the Supporting Information.

2.3. Fourier Transform Infrared Spectroscopy. Fourier transform infrared (FT-IR) spectra were measured using a Thermo-Fisher iS50 IR spectrometer with a resolution of 0.24 cm^{-1}. The absorption spectrum of PhSeCN in each sample was obtained by subtracting the background spectra of the same film without the probe.

2.4. SEM Characterization. The cryo-fractured cross area of the sample films was characterized using a Thermo Fisher Scientific

Apreo S LoVac scanning electron microscope. The SEM samples were sputter-coated with Au/Pd (60:40 ratio) to avoid charging. The SEM micrographs were collected in the immersion mode using a voltage of 20 kV and a current of 50 pA.

2.5. Polarization-Selective Pump Probe Experiment. A detailed description of the laser system has been presented previously.[45,46] In short, a Ti/sapphire oscillator seeded regenerative amplifier (regen) was used to generate 800 nm femtosecond pulses at a 3 kHz repetition rate with 2 mJ energy. The output from the regen was converted by a home-built tunable optical parametric amplifier and a difference frequency generator to the resonant frequency of the PhSeCN nitrile stretch (4.6 m, 30 μJ, 3 kHz). The final mid-IR pulses have a bandwidth of ~90 cm^{-1} and are close to transform-limited.

For polarization-selective pump-probe (PSPP) experiments, a strong polarized pump pulse passes through the sample first and excites a cosine-squared distribution of PhSeCN probe molecules along the pump polarization axis. The pump pulse, in effect, labels the initial orientations of the PhSeCN molecules. Then, after a variable time delay, t, a weaker probe pulse travels through the same spot on the sample to generate the signal, which is detected at polarization either parallel ($I_\parallel$) or perpendicular ($I_\perp$) to the pump pulse. The excited PhSeCN probe molecules can undergo partial reorientation within the sample during the time between the two pulses. By measuring the parallel and perpendicular signal intensities as a function of the delay time, the PSPP experiment can measure the orientational relaxation of the vibrational probes. The signal intensity is affected by both the probe's vibrational lifetime and the reorientation. The signals are a combination of the CN excited state population lifetime, $P(t)$, and the second Legendre polynomial orientational correlation function, $C_2(t)$[51,52]

$$I_\parallel = P(t)(1 + 0.8C_2(t))$$
$$I_\perp = P(t)(1 - 0.4C_2(t)) \tag{1}$$

Using the measured $I_\parallel$ and $I_\perp$, both population lifetime and anisotropy, $r(t)$, were obtained using

$$P(t) = \frac{1}{3}(I_\parallel(t) + 2I_\perp(t))$$

$$r(t) = \left(\frac{I_\parallel(t) - I_\perp(t)}{I_\parallel(t) + 2I_\perp(t)}\right) = 0.4C_2(t) \tag{2}$$

The main observable for the ROAM, the anisotropy, is proportional to the transition dipole's second Legendre polynomial orientational correlation function.

2.6. Restricted Orientation Anisotropy Method. A comprehensive description and explanation of how the ROAM works has been published previously.[44,46] Here, we include a brief overview of the methodology. ROAM utilizes the PSPP experiment described above to measure the orientational relaxation (anisotropy) of the vibrational probe molecules embedded in the FVEs across a range of frequencies within the inhomogeneously broadened absorption spectrum (FT-IR) of the CN stretching mode of the probe. In a glassy polymer, the probes can only sample a limited range of angles determined by the sizes of the polymer FVEs and the probe size. Therefore, the anisotropy can only decay to a nonzero constant offset. In addition, the anisotropy decays vary across the inhomogeneous distribution of absorption frequencies. The different decays correspond to subensembles of probes confined in different sizes of FVEs. Confining the probe in a smaller radius FVE subensemble results in less angular decay.

The anisotropy decay curves at each frequency are converted to half-cone angles by employing the wobbling-in-a-cone (WIAC) model.[53−56] In the WIAC model, the relationship of the observed anisotropy decays to the cone angles is exact. The relationship between the observed decay time constants and the orientational diffusion constants is approximate. Here, FVEs are treated as cylindrical elements, and the half-cone angles are the half-angles of the largest cone the probe can make inside the cylinder.[44] Detailed

experiments have shown that the ensemble-averaged shape of FVEs is a cylinder.[44] The parametrization is given in the following expression[57]

$$r(t) = 0.4S_0^2(S_1^2 + (1 - S_1^2)\exp(-t/\tau_1))$$
$$(S_2^2 + (1 - S_2^2)\exp(-t/\tau_2)) \tag{3}$$

S_0, S_1, and S_2 are order parameters describing the range of angular sampling, which can be converted to the cone angles using eq 4

$$S_i = \frac{1}{2}\cos(\theta_i)(1 + \cos(\theta_i)) \tag{4}$$

S_0S_1 is converted to θ_{fast}, which describes the fast diffusive motion that occurs at a time scale <10 ps. S_0 reflects the portion of the fast orientational relaxation that occurs within the time limited by the IR pulse duration. The order parameter can be obtained, but an associated time constant cannot be observed. θ_{fast} is the cone angle for the angular space sampled immediately available to the probe molecules, which is determined by the FVE sizes. A larger cone angle corresponds to a larger FVE size. $S_0S_1S_2$ is converted to θ_{tot}, corresponding to the maximum angular range sampled by the probe. Then, θ_{slow} is calculated as the difference between θ_{tot} and θ_{fast}

$$\theta_{slow} = \theta_{tot} - \theta_{fast} \tag{5}$$

θ_{slow} is attributed to angular samplings on a much longer time scale (usually >100 ps). θ_{slow} measures the additional angular space explored by the probes, which is associated with FVE surface topography fluctuations caused by the movement of the side chains.[44] In this study, only θ_{fast} is used in the analysis.

From the experiments, we obtain fast cone angles over a range of frequencies across the absorption spectrum. The fast cone angles are direct reflections of the FVE sizes. The cone angles can be converted into FVE radii using the contact geometries and dimensions of the probe molecule, PhSeCN. The following equation gives the conversion from cone angles to radii (R)

$$R = \frac{1}{2}(l\sin(\theta_{fast}) + \Delta r_1 + \Delta r_2) \tag{6}$$

l is the length of the PhSeCN from the center of the selenium (Se) atom to the center of the para-hydrogen and Δr_1 and Δr_2 are the van der Waal (vdW) radii of the Se atom and the para-hydrogen atom, respectively.[44] The value of l was determined from a density functional theory calculation. $l = 5.81$ Å. The vdW radii of Se and hydrogen atoms are obtained from the literature to be 2.12 and 1.0 Å, respectively.[58,59]

As mentioned above, the anisotropy decays (cone angles) are frequency-dependent. Therefore, the FVE radius also changes from one frequency to another of the CN stretch FT-IR spectrum. The spectrum is the frequency probability distribution. By combining the FVE radii measured at each frequency with the population distribution of frequencies from the FT-IR spectrum, the FVE RPD (RPD) can be determined using the principle of maximum entropy.[46] The expectation value of frequency-dependent FVE radii can be expressed using the following equation

$$\langle R(\omega)\rangle = \frac{1}{\rho(\omega)}\int_0^\infty \rho(\omega|R)\rho(R)R\,dR \tag{7}$$

where $\rho(\omega)$ is the area-normalized CN stretch FT-IR spectrum of the PhSeCN probes in the polymer samples. $\rho(\omega|R)$ is the conditional probability density function of PhSeCN molecules having a frequency ω, given that it is in an FVE of radius R. $\rho(R)$ is the RPD for the polymer of interest. $\rho(\omega|R)$ is taken to be Gaussian with exponentially increasing width with respect to decreasing radius, which is consistent with simulation results for PS oligomers.[46] The parameters for $\rho(\omega|R)$ are iterated to simultaneously reproduce the experimentally determined FT-IR spectrum, $\rho(\omega)$, and the FVE radius at each frequency, $\langle R(\omega)\rangle$. The generated RPD is robust because the fit is highly constrained by the experimental data.

C

3. RESULTS

Nanoparticles are prone to form aggregates due to their high surface energy.[50] Aggregation in the high filler content regime (>1 vol %) is commonly seen and is often regarded as the cause for the reduction of property enhancement.[7,60] Significant aggregation of nanofillers would decrease the interphase volume fraction,[61] rendering the measurement and calculation of the interphase properties inaccurate. Therefore, to rigorously examine the FVE radius distribution in the interfacial layer, we limited our study to well-distributed PANC samples with nanofiller concentrations up to 2% by weight (~0.67 vol %). Figure 1 displays cross-sectional SEM
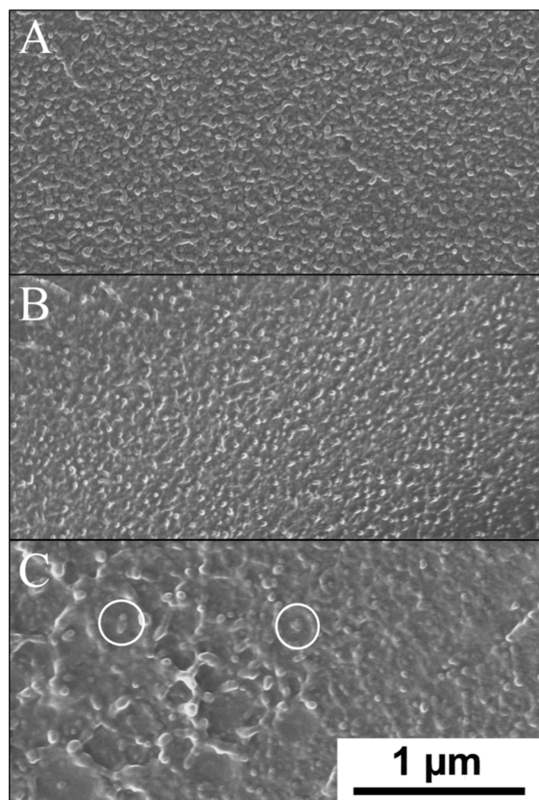
Figure 1. SEM micrographs of cryo-fractured cross-sections of PANCs containing (A) 0.5 wt %, (B) 1 wt %, and (C) 2 wt % 20 nm diameter Al_2O_3 nanoparticles. The white circles highlight a small number of aggregates in the 2 wt % sample.

micrographs of PANCs with filler weight fractions of 0.5, 1, and 2% (PANC-0.5, PANC-1, and PANC-2, respectively). Many micrographs were examined, and they all had the same appearance. The Al_2O_3 nanoparticles are almost all single particles in all three nanocomposite samples. They are homogeneously distributed with no large clusters of agglomeration, demonstrating excellent nanofiller dispersion. Although great efforts were made to ensure good dispersion, a few very small aggregates could still be observed for PANC-2 (Figure 1C, circled). In this case, given the small number and sizes of the aggregated clusters, they will have minimal impacts on the results.

The linear absorption spectrum of the CN stretching mode of PhSeCN embedded in PEI is shown in Figure 2. The spectrum is fit with a Gaussian function to obtain the center frequency and full widths at half-maximum (fwhms). The center frequency of the PhSeCN nitrile stretching mode in PEI
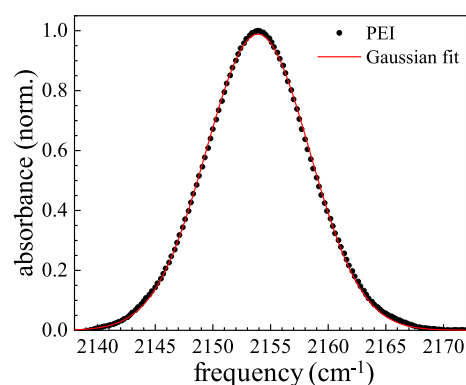
Figure 2. FT-IR spectrum of the PEI film. The red line is the Gaussian fit to the experimental spectrum.

is 2153.9 ± 0.1 cm^{-1} with fwhms of 9.0 ± 0.1 cm^{-1}. There were no discernible differences in the line shapes between the FT-IR spectrum of PEI and those of the PEI nanocomposites (Figure S2), which is consistent with the small quantities of nanoalumina that were added. As discussed below, PSPP spectroscopy is much more sensitive to variation in environments than FT-IR, and we do observe differences in the orientational dynamics of the probe molecule in different nanofiller concentration samples. The frequency of the ultrafast IR pulses for the anisotropy measurements is set to the center frequency from the FT-IR spectrum. The anisotropy data are collected at the center frequency as well as three frequencies on each side of the spectrum with ~1.5 cm^{-1} spacing.

The orientational dynamics of PhSeCN in a PEI sample are shown in Figure 3A for seven frequencies (2149.1 to 2158.2
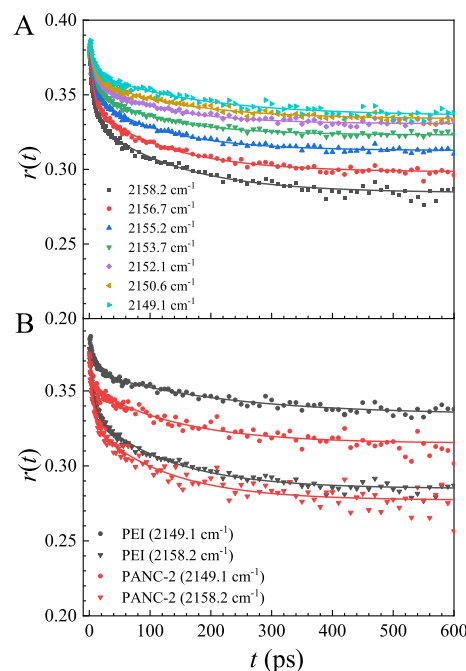


Figure 3. (A) Anisotropy decays of PhSeCN probes in PEI at seven frequencies across the inhomogeneously broadened spectrum. The decays are fit to the WIAC model, and they clearly exhibit strong frequency dependence. (B) Comparison of the anisotropy decay between pure PEI and PANC-2 at two different frequencies. At the lower frequency, the difference between the two decays is much greater.

cm^{-1}) to illustrate the anisotropy data's common features. The solids lines are the fits to the experimental data using the WIAC model (eq 3). The extent of the anisotropy provides a measurement of the angular range sampled by the probes. When the probe molecules are free to rotate, e.g., in a bulk liquid, all angles can be sampled, and the anisotropy decays from the theoretical maximum of 0.4 to 0.[62] However, when there are physical restrictions that block complete angular sampling, i.e., when the probe molecules are confined to FVEs, the anisotropy will decay to a nonzero offset because only a limited range of angles can be sampled. In Figure 3A, the anisotropy at each frequency decays to a distinct offset, demonstrating that the PhSeCNs experience different degrees of restriction from FVE subensembles at different frequencies. This phenomenon has been thoroughly described and explicated in the previous publications.[45,46] The PhSeCN molecules experience strong Stark coupling to their surrounding environments, that is, the CN stretch vibrational frequency is shifted by the electric field strengths in the FVEs experienced by the probe molecules.[63]

Experiments and simulations of PhSeCN in PS oligomers have shown that subensembles of PhSeCNs in small FVEs experience larger electric fields than those in larger FVEs.[45,46] As the electric field increases, the CN stretch frequency is shifted to the red. Therefore, frequency-dependent anisotropies are measurements of the orientational dynamics of PhSeCN in FVEs of different sizes. On the high frequency (blue) side of the absorption line, the FVEs are large and become progressively smaller as the frequency shifts to a lower frequency (red). This frequency dependence of the FVE size is central to the determination of the RPD curves.

Examining specific trends (Figure 3A), the greater extents of decays are observed in the anisotropies at higher frequencies, which means that $r(t)$ at higher frequencies measures PhSeCN subensembles in larger FVEs. Changes in the anisotropy decays are also caused by the addition of nano-Al$_2$O$_3$ particles. The changes in the anisotropy decays will be described for different amounts of 20 nm nano-Al$_2$O$_3$ added to the polymer matrix. To demonstrate the differences, the anisotropies of PEI and PANC-2 at two different frequencies are shown in Figure 3B. The anisotropy data for PANC-2 decay more than those for PEI at both 2149.1 and 2158.2 cm^{-1}. The difference between the anisotropies at 2149.1 cm^{-1} is much larger than the difference at 2158.2 cm^{-1}. This result indicates that the subensembles corresponding to the lower frequencies (smaller FVEs) are affected more by the addition of nano-Al$_2$O$_3$ particles. The same trends are observed for all nanocomposite samples, and the amount of change is directly correlated with the added weight fraction of the alumina nanoparticles.

The complete frequency-dependent anisotropy data for all three PANC samples are given in Figure S3. The FVE radii change with frequencies are apparent after the anisotropy decays have been converted to radii using eqs 3, 4, and 6. The FVE radii vs frequency are displayed in Figure 4. The change in the FVE radii between 2149.1 and 2158.2 cm^{-1} becomes smaller as the nanoparticle concentration increases. As discussed below, because the distribution of the frequencies (FT-IR spectra as in Figure 2) is virtually identical for samples with different concentrations of nanoparticles (see Figure S2), the FVE RPD for the nanocomposites with all nanoparticle concentrations studied is substantially narrower than that found for the bulk sample.
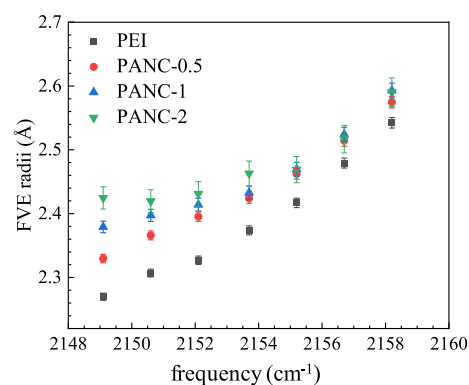
Figure 4. Frequency-dependent FVE radii for PEI, PANC-0.5, PANC-1, and PANC-2. With increasing nanofiller fraction, increases in the radii are observed across various frequencies, although the radii at lower frequencies experience a greater amount of change.

The FVE RPDs are determined by simultaneously fitting the distribution of frequencies (FT-IR, Figure 2) and the FVE radius at each frequency (Figure 4) using the maximum entropy method discussed in Section 2.6. This method does not assume a functional form for the shape of the distribution, which is important in the analysis presented below. The area-normalized RPD curves for all four films are presented in Figure 5A. The RPDs for all four samples exhibit non-Gaussian distribution characterized by the tails extending toward larger radii. Significant differences in the shape of the distribution are observed between the PEI and PANC samples. For PEI, the average radius determined from the RPD is 2.43 Å, and the
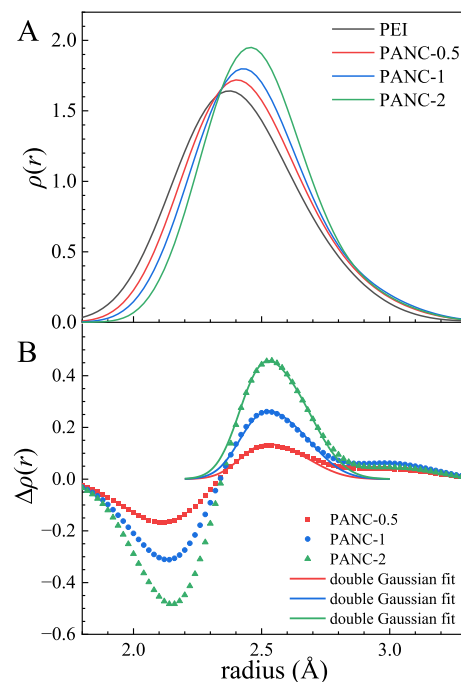
Figure 5. (A) Area-normalized FVE RPDs for PEI, PANC-0.5, PANC-1, and PANC-2. With increasing nanofiller content, the peaks of the distributions shift toward the large radius side and the width becomes progressively narrower. (B) RPD difference between the PANCs and the PEI. The positive peaks at ~2.5 Å have approximately the same shapes. The three curves are simultaneously fitted with the sum of two Gaussians to extract the interphase FVE distribution. All parameters for the fit are shared except for the peak areas.

peak of the distribution is at 2.38 Å with an fwhm of 0.56 Å. With the addition of 0.5, 1, and 2% weight fractions, the average radius increased to 2.46, 2.49, and 2.51 Å, respectively. The peaks of the RPDs are slightly shifted to 2.40, 2.42, and 2.46 Å, respectively. As anticipated in the earlier discussion of Figure 4, the width of the distribution progressively narrows with the increasing concentration of nano-Al_2O_3. The fwhm for PANC-0.5, PANC-1, and PANC-2 decreased to 0.54, 0.51, and 0.47 Å, respectively. Table 1 provides a summary of the

Table 1. Summary of the Average Radii (R_{avg}), Maximum Radii (R_{max}), and fwhm for the FVE RPDs

	R_{avg} (Å)	R_{max} (Å)	fwhm (Å)
PEI	2.43	2.38	0.56
PANC-0.5	2.46	2.40	0.54
PANC-1	2.49	2.42	0.51
PANC-2	2.51	2.46	0.47

average, maximum, and fwhm values for the RPDs. In the following section, a quantitative analysis of the changes in RPDs is conducted to determine the distribution of the FVE radii in the interfacial layer and use these results to determine the interfacial layer thickness.

4. DISCUSSION

4.1. Interfacial Layer Analysis. The majority of the property improvements of PNCs have been attributed to the changes in the polymer structure and properties of the interphase.[21] Differences between the interphase and bulk chain arrangements would be expected to and, as shown below, influence the interphase FVEs. The changes in the FVE RPDs are used to obtain properties of the interphase region. If the interfacial regions of individual nanoparticles do not overlap in the low filler content regime, then the shape of the RPD for the interphase should not change with nanoparticle concentration. Based on calculations using the interface volume model,[25] all samples discussed in this study are in the low-concentration regime as long as the interfacial layer thickness is ≤30 nm. The details of the calculation are presented below, and it will be shown that the final result does meet this condition.

To illustrate the changes in the distributions, the differences of the area-normalized RPDs between PEI and its nanocomposites are presented in Figure 5B, i.e., the PEI RPD is subtracted from the other RPDs. Consistent with the direct observation of the RPD shapes, a reduction in probability is evident on the smaller radius side (<2.35 Å). The RPDs are area normalized, so the integral of the positive peak is equal to that of the negative area. Since the increased areas are the distributions not present in the neat PEI sample, they have to be generated from the influence of the interfacial layer. The positive peaks have essentially the same center and shape regardless of the nanofiller content, which agrees with our earlier argument that the distribution in the interfacial area should be independent of the nanofiller content for relatively low concentrations. Additionally, positive correlations are seen between the peak area and the nanofiller content. The peaks at ~2.5 Å were analyzed to extract the characteristics of the interface.

The shape of the positive features resembles a Gaussian distribution for smaller radii with a tail to the large radius side. The non-Gaussian shape can be modeled as the sum of two Gaussians. Note that this model is only used to extract the

distribution shape and is not intended to indicate that the shape is the sum of two distinct Gaussians. To ensure that the fits to the peaks for the three concentrations have the same shape, the center frequencies and the fwhm of each Gaussian were shared. Additionally, the area ratio of the two Gaussian was also constrained. As can be seen from Figure 5B, the simultaneous fits across the three peaks reproduce the shapes very well. The fitted curves are good approximations of the RPD in the interfacial layer. They are area-normalized and compared to the RPD of neat PEI in Figure 6. The distribution
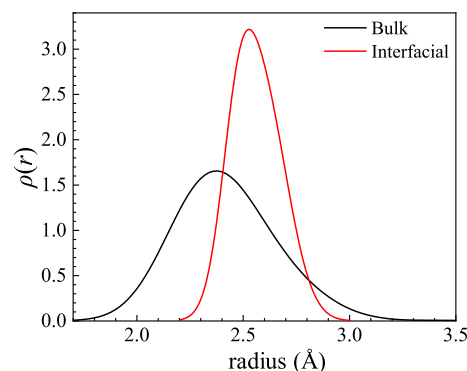
Figure 6. Comparison between the FVE RPD of bulk PEI (black curve) and the RPD at the interfacial layer (red curve). The interfacial RPD is shifted to a larger radius side and is much narrower than in the bulk.

in the interfacial layer is much narrower than in the bulk, and the average radius shifts from 2.43 to 2.55 Å as a result of the elimination of smaller radii FVEs. This indicates that the presence of nanoparticles disrupts polymer chain packing in a way that predominantly affects smaller FVEs, although the long tail to large radii found in the bulk RPD is also eliminated. Furthermore, the total areas from the fits are equivalent to the volume fractions of the interfacial layer, which are 4.2, 8.2, and 14.2% for PANC-0.5, PANC-1, and PANC-2, respectively. According to Raetzke's interfacial volume model,[25] the interfacial volume content increases linearly with the nanofiller volume fraction for low filler content because interfacial layers do not overlap. The range of validity is $\frac{2}{\sqrt{3}}(d + 2i) \leq a_0$, where d is the nanofiller diameter, i is the interfacial layer thickness, and a_0 is the distance between the centers of neighboring nanoparticles. a_0 can be calculated based on the nanofiller volume fraction (p) and the nanofiller diameter (d) using the following equation assuming random distribution[21]

$$a_0 = d\left(\frac{2}{\pi \cdot p}\right)^{1/3} \tag{8}$$

For the highest alumina nanoparticle content sample (0.65 vol %), a_0 is determined to be 92 nm. Then, the range of validity is satisfied as long as $i \leq 30$ nm. The interphase fraction (p_i) can be expressed as

$$p_i = p\left[\left(1 + \frac{2i}{d}\right)^3 - 1\right] \tag{9}$$

The interphase volume percentage vs nanofiller volume percentage plot is given in Figure 7, where the red line is the linear fit to the data with the condition that the interphase fraction is zero when the nanofiller fraction is zero. A
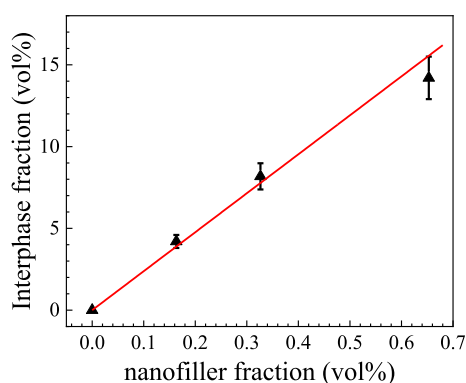
Figure 7. Interphase volume fraction determined from the change in RPD vs the nanofiller volume fraction. The red line is the fit to the interphase volume model for low filler content. The interfacial layer thickness is determined to be 19.2 ± 0.5 nm from the slope.

significant result from the plot in Figure 7 is that the interphase layer thickness (i) determined from the slope is 19.2 ± 0.5 nm. It is interesting to compare the interphase layer thickness to the radius of gyration of the polymer. The PEI used in this study has a melt index of 9 g/10 min, which is equivalent to molecular weight of ∼52 kg/mol.[64] The radius of gyration measured by light scattering for similar polyimides with the same molecular weight ranges from 15 to 25 nm.[65] Although it is a rough estimate, it shows that the interphase thickness is comparable to the radius of gyration. However, this radius of gyration estimate applies to pure PEI. As shown in Figure 6, the RPD for the interfacial region is very different from that of pure PEI. A change in the RPD is caused by changes in the polymer structure in the vicinity of the nanoparticles. It is likely that the radius of gyration near the nanoparticles is different from that of the bulk material.

4.2. Comparison to the Literature: The Interfacial Layer Thickness. The ROAM is a robust technique with the first principles theory underpinning the analysis of FVE radii and the RPD. In a recent paper,[44] it was demonstrated that the same size FVEs were measured in PS using six different vibrational probes. The six probes had different lengths and shapes, demonstrating that the results are independent of the particular probe. There is a single assumption in the method, that is, the ensemble average FVE shape is cylindrical. This assumption was verified because the cylindrical shape is necessary for the six probes to give the same FVE radius. The determination of the RPD requires that it simultaneously reproduces both the measured frequency-dependent radii and the FT-IR spectrum of the mode of the vibrational probe used in the measurements. The requirement to reproduce two independent observables is a severe constraint, which supports the accuracy of the results.

The RPD presented in Figure 6 indicates that the transition from the interphase to bulk is closer to abrupt than gradual. Were the transition gradual, the interphase RPD would be an average over a range of subensemble distributions that were increasingly close to the bulk distribution. Therefore, the interphase RPD would be expected to contain the full range of radii of the bulk distribution but with lower probabilities in some regions. The complete absence of bulk FVE radii in the small radius portion of the distribution demonstrates that the transition is reasonably abrupt. The linear plot in Figure 7 with the intercept at zero is based on the multilayer core–shell model.[23] Although the ROAM result cannot distinguish

between different types of layers, the interphase RPD indicates a rapid transition between the perturbed and bulk regions. Therefore, the line through the data should provide an accurate determination of the shell thickness, 19.2 ± 0.5 Å.

It is interesting to compare the results of the experiments and analysis presented here to other techniques from the literature. Because the interphase has no directly observable boundary to separate it from the bulk polymer[66] and the interphase thickness will depend on the specific nanofiller–polymer interactions, the measurements of the interfacial layer thickness values from the literature are varied. For the current system of interest, the interfacial interaction between PEI and alumina nanoparticles is considered weakly attractive.[67] In addition, Tanaka's multicore model states that there are different types of interfacial layers with different thicknesses.[23] Specifically, the estimated thickness for the bonded layer is ∼1 nm, while the "bound layer" and "loose layer" can be tens of nanometers.

On the smaller end of measured interphase thicknesses, SAXS usually reports interfacial layers of ∼2 nm.[28,30−32] For example, Li et al. investigated the interphase structure of the polyimide/Al_2O_3 nanocomposite using SAXS. The interfacial layer thickness is determined using the sigmoidal density profile model to be ∼1−2 nm.[68] Genix et al. studied the poly(vinyl acetate) silica nanocomposites with various dispersion states and found that the interfacial layer has ∼10% reduced density and a thickness of approximately 2 nm for ideally dispersed samples.[31] BDS is another commonly used technique for investigating interfacial layer properties in nanocomposites.[33] Klonos and co-workers conducted a BDS study on poly(dimethylsiloxane)/titania nanocomposites prepared by sol−gel or solvent casting.[35] Their analysis showed that the segmental relaxation in the interfacial layer was significantly slowed down, and the thickness of the interface was determined to be 9 and 5 nm for the nanocomposites made by the sol−gel method and solvent casting, respectively. The BDS characterization of poly(2-vinylpyridine)/silica nanocomposites by Holt and colleagues detected an interfacial layer with ∼100 times slower relaxation process, and the thickness of such a layer is estimated to be 4−6 nm independent of the nanofiller fraction.[69]

Microscopy-based techniques usually detect the interfacial layer thickness to be upward of 10 nm.[29] Using a combination of AFM and electric force microscopy, Seiler and Kindersberger showed that the interphase thickness is ∼40 nm for nanocomposite materials composed of a silicone matrix and hydrophilic silica as nanofillers.[70] The authors also measured the resistance to high voltage arcing for the same nanocomposites with different filler contents, and the effective interphase thickness was estimated to be 25−30 nm using the interphase volume model calculation.[70] Houssat et al. utilized the AFM peak force quantitative nanomechanical (PF QNM) mode to characterize the interfacial mechanical properties of polyimide/Si_3N_4 nanocomposites.[37] A significant increase in Young's modulus was detected near the Si_3N_4 nanoparticles, and the interphase thickness of 27 nm was reported.

Although PALS has been employed to measure the FVE properties for many PNC systems, the effective interfacial layer thickness is only occasionally estimated from PALS measurements. Ohrt and co-workers used focused positron beams to perform PALS measurements at the interface between a Teflon AF 1600 film and a silicon nitride membrane.[71] o-Ps lifetimes are measured as a function of the implantation depth of the

positron beam, and the interfacial layer thickness is estimated to be 12 nm. Similarly, Jean et al. measured the o-Ps annihilation lifetime in the interface between amorphous PS and a Si substrate.[72] Reduced density was observed in the interfacial region, and the interface thickness was reported to be 21 ± 3 nm. It is worth noting that the interface between a planar material and a polymer is not likely to be the same as with a small spherical particle.

In this study, ROAM measurements determined that the interphase thickness is 19.2 ± 0.5 nm, agreeing quite well with the AFM[37] and PALS[71,72] estimations. In contrast, SAXS and BDS measurements report much thinner layers. The terms "interphase" and "interfacial layer" in the literature often do not distinguish between the different layers defined in the multicore model. Likely, SAXS and BDS can only observe the bonded layer, where polymer chains are strongly absorbed to the nanoparticle surface. It has been proposed that the effects of the nanofiller surface extend well beyond the bonded layer.[73,74] Zhang et al. performed multiscaled simulations on PANCs to extract the morphology and dielectric properties.[75] Coarse-grained MD simulation revealed that PANCs experienced a significant reduction in density, and additional voids appeared between polymer chains beyond the immediate vicinity of the nanoparticles. Although the reduction in density is not equivalent to increased FVE radii, the simulation results support our observation that the effective interfacial layer thickness is relatively large for PEI nanocomposites.

5. CONCLUDING REMARKS

The FVE radii and the RPDs were determined for PEI containing 0−2 wt % well-dispersed 20 nm Al_2O_3 nanoparticles using the ultrafast IR spectroscopy technique, ROAM. The FVE characteristics are significantly altered in the nanocomposites. The addition of the nanoparticles causes the RPD to narrow substantially and shift to a larger average radius. The substantial narrowing of the RPD occurs mainly on the small radius side of the distribution. The fact that a wide range of small FVEs occur in pure PEI and are absent in the interphase layer indicates that the transition from the interphase to the bulk is quite abrupt. If there were a continuous gradual transition from a highly perturbed polymer structure to the bulk structure, the RPD would reflect an average of structures, including some probability for those close to the bulk structure.

By subtracting the pure PEI RPD from the RPDs obtained from different concentrations of nanoparticles, the interphase FVE RPDs were obtained. For concentrations of 0.5, 1, and 2%, the shapes of the interphase RPDs are identical within a small experimental error, demonstrating that at even the highest concentration studied, the interphase layers are not overlapping. The interphase volume fractions were determined using the area of the interface RPDs for each concentration. Our results show that the interphase volume fraction increases linearly with the nanofiller content, and the interfacial layer thickness is 19.2 ± 0.5 nm using the interphase volume model for the low filler content regime.[25]

PEI is an important high-temperature dielectric material. Many previous studies have found that adding small amounts of low-dielectric-constant nanofiller substantially improves the dielectric properties of the PEI films.[7,9,10] Here, we have provided a detailed analysis of how spherical nanoparticles impact polymer chain packing in PEI. The relatively large interphase layer thickness (~19 nm) found in this study can potentially explain why a very small volume fraction of nanoparticles significantly impacts the bulk property. This knowledge regarding the microscopic origin of bulk properties can be useful for the rational design of functional PNC materials.

The current study also demonstrates the ROAM measurements' high spatial resolution and sensitivity to different modifications of the polymer matrix. This technique can be applied to systems other than the PEI/Al_2O_3 nanocomposites. The two main considerations for implementing the ROAM are optical quality and the vibrational probes. First, the polymer films should be optically transparent and free from optical birefringence. Therefore, the application of the ROAM is mainly limited to transparent amorphous polymers. There are no inherent limitations for the types/sizes of nanoparticles as long as they do not introduce a large amount of scattering. In addition, ROAM measurements utilize the vibrational probe, phenyl selenocyanate; however, other probe molecules can be used.[44] The polymer needs to contain the probe molecules over an extended period. Depending on the specific types of polymers, the probes can diffuse out of the polymer matrix at elevated temperatures. Therefore, an appropriate probe that suits the particular polymer system under study should be selected. ROAM data acquisition is generally limited to temperatures below the glass transition temperature (T_g), although it is possible to perform studies above but close to T_g.

■ ASSOCIATED CONTENT

ⓢ Supporting Information

The Supporting Information is available free of charge at https://pubs.acs.org/doi/10.1021/acs.macromol.4c00868.

> NMR spectra, linear absorption spectrum, and frequency-dependent anisotropy decays (PDF)

■ AUTHOR INFORMATION

Corresponding Author

Michael D. Fayer − *Department of Chemistry, Stanford University, Stanford, California 94305, United States;* ⓞ orcid.org/0000-0002-0021-1815; Phone: 650 723-4446; Email: fayer@stanford.edu

Authors

Junkun Pan − *Department of Chemistry, Stanford University, Stanford, California 94305, United States;* ⓞ orcid.org/0000-0001-6128-1844

Aaron P. Charnay − *Department of Chemistry, Stanford University, Stanford, California 94305, United States;* ⓞ orcid.org/0000-0003-1797-9465

Complete contact information is available at:
https://pubs.acs.org/10.1021/acs.macromol.4c00868

Notes

The authors declare no competing financial interest.

■ ACKNOWLEDGMENTS

■ REFERENCES

(1) Fukushima, Y.; Inagaki, S. Synthesis of an intercalated compound of montmorillonite and 6-polyamide. *J. Inclusion Phenom.* **1987**, *5*, 473−482.

(2) Mazeiko, V.; Kausaite-Minkstimiene, A.; Ramanaviciene, A.; Balevicius, Z.; Ramanavicius, A. Gold nanoparticle and conducting polymer-polyaniline-based nanocomposites for glucose biosensor design. *Sens. Actuators, B* **2013**, *189*, 187−193.

(3) Song, Q.; Nataraj, S. K.; Roussenova, M. V.; Tan, J. C.; Hughes, D. J.; Li, W.; Bourgoin, P.; Alam, M. A.; Cheetham, A. K.; Al-Muhtaseb, S. A.; et al. Zeolitic imidazolate framework (ZIF-8) based polymer nanocomposite membranes for gas separation. *Energy Environ. Sci.* **2012**, *5*, 8359.

(4) Cong, H.; Radosz, M.; Towler, B.; Shen, Y. Polymer-inorganic nanocomposite membranes for gas separation. *Sep. Purif. Technol.* **2007**, *55*, 281−291.

(5) Chen, Q.; Shen, Y.; Zhang, S.; Zhang, Q. M. Polymer-Based Dielectrics with High Energy Storage Density. *Annu. Rev. Mater. Res.* **2015**, *45*, 433−458.

(6) Choudhury, A. Dielectric and piezoelectric properties of polyetherimide/BaTiO3 nanocomposites. *Mater. Chem. Phys.* **2010**, *121*, 280−285.

(7) Ren, L.; Yang, L.; Zhang, S.; Li, H.; Zhou, Y.; Ai, D.; Xie, Z.; Zhao, X.; Peng, Z.; Liao, R.; et al. Largely enhanced dielectric properties of polymer composites with HfO2 nanoparticles for high-temperature film capacitors. *Compos. Sci. Technol.* **2021**, *201*, 108528.

(8) Fan, M.; Hu, P.; Dan, Z.; Jiang, J.; Sun, B.; Shen, Y. Significantly increased energy density and discharge efficiency at high temperature in polyetherimide nanocomposites by a small amount of Al2O3 nanoparticles. *J. Mater. Chem. A* **2020**, *8*, 24536−24542.

(9) Thakur, Y.; Zhang, T.; Iacob, C.; Yang, T.; Bernholc, J.; Chen, L. Q.; Runt, J.; Zhang, Q. M. Enhancement of the dielectric response in polymer nanocomposites with low dielectric constant fillers. *Nanoscale* **2017**, *9*, 10992−10997.

(10) Zhang, T.; Thakur, Y.; Zhang, Q. M. Doped dielectric polymers with low dielectric constant nanofillers. *2017 IEEE Conference on Electrical Insulation and Dielectric Phenomena*, 2017; pp 437−440.

(11) Winey, K. I.; Vaia, R. A. Polymer Nanocomposites. *MRS Bull.* **2007**, *32*, 314−322.

(12) Shan, S.; Chen, X.; Xi, Z.; Yu, X.; Qu, X.; Zhang, Q. The effect of nitrile-functionalized nano-aluminum oxide on the thermomechanical properties and toughness of phthalonitrile resin. *High Perform. Polym.* **2017**, *29*, 113−123.

(13) Li, J.; Liu, H.; Guo, J.; Hu, Z.; Wang, Z.; Wang, B.; Liu, L.; Huang, Y.; Guo, Z. Flexible, conductive, porous, fibrillar polymer-gold nanocomposites with enhanced electromagnetic interference shielding and mechanical properties. *J. Mater. Chem. C* **2017**, *5*, 1095−1105.

(14) Oh, H.; Green, P. F. Polymer chain dynamics and glass transition in athermal polymer/nanoparticle mixtures. *Nat. Mater.* **2009**, *8*, 139−143.

(15) Huang, X.; Jiang, P.; Xie, L. Ferroelectric polymer/silver nanocomposites with high dielectric constant and high thermal conductivity. *Appl. Phys. Lett.* **2009**, *95*, 242901.

(16) Liu, T.; Tong, Y.; Zhang, W.-D. Preparation and characterization of carbon nanotube/polyetherimide nanocomposite films. *Compos. Sci. Technol.* **2007**, *67*, 406−412.

(17) Ramanathan, T.; Liu, H.; Brinson, L. C. Functionalized SWNT/polymer nanocomposites for dramatic property improvement. *J. Polym. Sci., Part B: Polym. Phys.* **2005**, *43*, 2269−2279.

(18) Dwivedi, M.; Dixit, A.; Alam, S.; Ghosh, A. K. Dielectric and tensile behavior of nanoclay reinforced polyetherimide nanocomposites. *J. Appl. Polym. Sci.* **2011**, *122*, 1040−1046.

(19) Zhang, M. Q.; Rong, M. Z.; Pan, S. L.; Friedrich, K. Tensile Properties of Polypropylene Filled with Nanoscale Calcium Carbonate Particles. *Adv. Compos. Lett.* **2019**, *11*, 096369350201100.

(20) Lewis, T. J. Nanometric dielectrics. *IEEE Trans. Dielectr. Electr. Insul.* **1994**, *1*, 812−825.

(21) Huang, J.; Zhou, J.; Liu, M. Interphase in Polymer Nanocomposites. *JACS Au* **2022**, *2*, 280−291.

(22) Lewis, T. J. Interfaces: nanometric dielectrics. *J. Phys. D: Appl. Phys.* **2005**, *38*, 202−212.

(23) Tanaka, T.; Kozako, M.; Fuse, N.; Ohki, Y. Proposal of a multi-core model for polymer nanocomposite dielectrics. *IEEE Trans. Dielectr. Electr. Insul.* **2005**, *12*, 669−681.

(24) Raetzke, S.; Kindersberger, J. Role of interphase on the resistance to high-voltage arcing, on tracking and erosion of silicone/SiO2 nanocomposites. *IEEE Trans. Dielectr. Electr. Insul.* **2010**, *17*, 607−614.

(25) Raetzke, S.; Kindersberger, J. The Effect of Interphase Structures in Nanodielectrics. *IEEJ Trans. Fund. Mater.* **2006**, *126*, 1044−1049.

(26) Andritsch, T.; Kochetov, R.; Morshuis, P. H. F.; Smit, J. J. Proposal of the polymer chain alignment model. *2011 Annual Report Conference on Electrical Insulation and Dielectric Phenomena*, 2011.

(27) Lewis, T. J. Interfaces are the dominant feature of dielectrics at the nanometric level. *IEEE Trans. Dielectr. Electr. Insul.* **2004**, *11*, 739−753.

(28) Cheng, S.; Carroll, B.; Bocharova, V.; Carrillo, J. M.; Sumpter, B. G.; Sokolov, A. P. Focus: Structure and dynamics of the interfacial layer in polymer nanocomposites with attractive interactions. *J. Chem. Phys.* **2017**, *146*, 203201.

(29) Wang, S.; Luo, Z.; Liang, J.; Hu, J.; Jiang, N.; He, J.; Li, Q. Polymer Nanocomposite Dielectrics: Understanding the Matrix/Particle Interface. *ACS Nano* **2022**, *16*, 13612−13656.

(30) Singh, P. S. Small-Angle Scattering Techniques (SAXS/SANS). *Membrane Characterization*; Elsevier, 2017, pp 95−111. DOI: 10.1016/B978-0-444-63776-5.00006-1.

(31) Genix, A. C.; Bocharova, V.; Carroll, B.; Lehmann, M.; Saito, T.; Krueger, S.; He, L.; Dieudonne-George, P.; Sokolov, A. P.; Oberdisse, J. Understanding the Static Interfacial Polymer Layer by Exploring the Dispersion States of Nanocomposites. *ACS Appl. Mater. Interfaces* **2019**, *11*, 17863−17872.

(32) Cheng, S.; Carroll, B.; Lu, W.; Fan, F.; Carrillo, J.-M. Y.; Martin, H.; Holt, A. P.; Kang, N.-G.; Bocharova, V.; Mays, J. W.; et al. Interfacial Properties of Polymer Nanocomposites: Role of Chain Rigidity and Dynamic Heterogeneity Length Scale. *Macromolecules* **2017**, *50*, 2397−2406.

(33) Cheng, S. Broadband Dielectric Spectroscopy of Polymer Nanocomposites. *Broadband Dielectric Spectroscopy: A Modern Analytical Technique*; ACS Symposium Series; American Chemical Society, 2021; pp 157−183.

(34) Carroll, B.; Cheng, S.; Sokolov, A. P. Analyzing the Interfacial Layer Properties in Polymer Nanocomposites by Broadband Dielectric Spectroscopy. *Macromolecules* **2017**, *50*, 6149−6163.

(35) Klonos, P.; Kyritsis, A.; Bokobza, L.; Gun'ko, V. M.; Pissis, P. Interfacial effects in PDMS/titania nanocomposites studied by thermal and dielectric techniques. *Colloids Surf., A* **2017**, *519*, 212−222.

(36) Aoyama, S.; Park, Y. T.; Macosko, C. W.; Ougizawa, T.; Haugstad, G. AFM probing of polymer/nanofiller interfacial adhesion and its correlation with bulk mechanical properties in a poly(ethylene terephthalate) nanocomposite. *Langmuir* **2014**, *30*, 12950−12959.

(37) Houssat, M.; Lahoud Dignat, N.; Cambronne, J.-P.; Diaham, S. AFM Measurements of Polyimide/Silicon Nitride Nanocomposite Interphase. *IEEE Trans. Nanotechnol.* **2018**, *17*, 1146−1150.

(38) Huang, H.; Dobryden, I.; Thorén, P. A.; Ejenstam, L.; Pan, J.; Fielden, M. L.; Haviland, D. B.; Claesson, P. M. Local surface mechanical properties of PDMS-silica nanocomposite probed with Intermodulation AFM. *Compos. Sci. Technol.* **2017**, *150*, 111−119.

(39) Xia, W.; Song, J.; Hsu, D. D.; Keten, S. Understanding the Interfacial Mechanical Response of Nanoscale Polymer Thin Films via Nanoindentation. *Macromolecules* **2016**, *49*, 3810−3817.

(40) Utpalla, P.; Sharma, S. K.; Prakash, J.; Bahadur, J.; Sahu, M.; Pujari, P. K. Free volume structure at interphase region of poly(ethylene oxide)-Al2O3 nanorods composites based solid polymer electrolyte and its direct correlation with Li ion conductivity. *Solid State Ionics* **2022**, *375*, 115840.

(41) Harms, S.; Rätzke, K.; Faupel, F.; Schneider, G. J.; Willner, L.; Richter, D. Free Volume of Interphases in Model Nanocomposites Studied by Positron Annihilation Lifetime Spectroscopy. *Macromolecules* **2010**, *43*, 10505−10511.

(42) Sharma, S. K.; Sudarshan, K.; Sahu, M.; Pujari, P. K. Investigation of free volume characteristics of the interfacial layer in poly(methyl methacrylate)-alumina nanocomposite and its role in thermal behaviour. *RSC Adv.* **2016**, *6*, 67997−68004.

(43) Cheng, X.; Putz, K. W.; Wood, C. D.; Brinson, L. C. Characterization of local elastic modulus in confined polymer films via AFM indentation. *Macromol. Rapid Commun.* **2015**, *36*, 391−397.

(44) Pan, J.; Charnay, A. P.; Fica-Contreras, S. M.; Fayer, M. D. Restricted Orientation Anisotropy Method for FVE Radii Characterization: Confirmed and Refined via the Study of Six Vibrational Probes. *Macromolecules* **2024**, *57*, 903−915.

(45) Hoffman, D. J.; Fica-Contreras, S. M.; Fayer, M. D. Amorphous polymer dynamics and free volume element size distributions from ultrafast IR spectroscopy. *Proc. Natl. Acad. Sci. U.S.A.* **2020**, *117*, 13949−13958.

(46) Fica-Contreras, S. M.; Hoffman, D. J.; Pan, J.; Liang, C.; Fayer, M. D. Free Volume Element Sizes and Dynamics in Polystyrene and Poly(methyl methacrylate) Measured with Ultrafast Infrared Spectroscopy. *J. Am. Chem. Soc.* **2021**, *143*, 3583−3594.

(47) Fica-Contreras, S. M.; Li, Z.; Alamri, A.; Charnay, A. P.; Pan, J.; Wu, C.; Lockwood, J. R.; Yassin, O.; Shukla, S.; Sotzing, G.; et al. Synthetically tunable polymers, free volume element size distributions, and dielectric breakdown field strengths. *Mater. Today* **2023**, *67*, 57−67.

(48) Olson, B. G.; Prodpran, T.; Jamieson, A. M.; Nazarenko, S. Positron annihilation in syndiotactic polystyrene containing α and β crystalline forms. *Polymer* **2002**, *43*, 6775−6784.

(49) Liu, J.; Deng, Q.; Jean, Y. C. Free-Volume Distributions of Polystyrene Probed by Positron-Annihilation - Comparison with Free-Volume Theories. *Macromolecules* **1993**, *26*, 7149−7155.

(50) Nguyen, V. S.; Rouxel, D.; Hadji, R.; Vincent, B.; Fort, Y. Effect of ultrasonication and dispersion stability on the cluster size of alumina nanoscale particles in aqueous solutions. *Ultrason. Sonochem.* **2011**, *18*, 382−388.

(51) Tokmakoff, A. Orientational correlation functions and polarization selectivity for nonlinear spectroscopy of isotropic media. I. Third order. *J. Chem. Phys.* **1996**, *105*, 1−12.

(52) Tan, H.-S.; Piletic, I. R.; Fayer, M. D. Polarization selective spectroscopy experiments: methodology and pitfalls. *J. Opt. Soc. Am. B* **2005**, *22*, 2009.

(53) Lipari, G.; Szabo, A. Effect of librational motion on fluorescence depolarization and nuclear magnetic resonance relaxation in macromolecules and membranes. *Biophys. J.* **1980**, *30*, 489−506.

(54) Lipari, G.; Szabo, A. Model-free approach to the interpretation of nuclear magnetic resonance relaxation in macromolecules. 1. Theory and range of validity. *J. Am. Chem. Soc.* **1982**, *104*, 4546−4559.

(55) Tan, H. S.; Piletic, I. R.; Fayer, M. D. Orientational dynamics of water confined on a nanometer length scale in reverse micelles. *J. Chem. Phys.* **2005**, *122*, 174501.

(56) Wang, C. C.; Pecora, R. Time-correlation functions for restricted rotational diffusion. *J. Chem. Phys.* **1980**, *72*, 5333−5340.

(57) Kramer, P. L.; Giammanco, C. H.; Fayer, M. D. Dynamics of water, methanol, and ethanol in a room temperature ionic liquid. *J. Chem. Phys.* **2015**, *142*, 212408.

(58) Bondi, A. van der Waals Volumes and Radii. *J. Phys. Chem.* **1964**, *68*, 441−451.

(59) Batsanov, S. S. Van der Waals Radii of Elements. *Inorg. Mater.* **2001**, *37*, 871−885.

(60) Miao, W.; Chen, H.; Pan, Z.; Pei, X.; Li, L.; Li, P.; Liu, J.; Zhai, J.; Pan, H. Enhancement thermal stability of polyetherimide-based nanocomposites for applications in energy storage. *Compos. Sci. Technol.* **2021**, *201*, 108501.

(61) Ashraf, M. A.; Peng, W.; Zare, Y.; Rhee, K. Y. Effects of Size and Aggregation/Agglomeration of Nanoparticles on the Interfacial/Interphase Properties and Tensile Strength of Polymer Nanocomposites. *Nanoscale Res. Lett.* **2018**, *13*, 214.

(62) Charnay, A. P.; Pan, J.; Fayer, M. D. Influence of Internal Bond Rotation on Ultrafast IR Anisotropy Measurements and the Internal Rotational Potential. *J. Phys. Chem. B* **2024**, *128*, 280−286.

(63) Fica-Contreras, S. M.; Charnay, A. P.; Pan, J.; Fayer, M. D. Rethinking Vibrational Stark Spectroscopy: Peak Shifts, Line Widths, and the Role of Non-Stark Solvent Coupling. *J. Phys. Chem. B* **2023**, *127*, 717−731.

(64) Sanner, M. A.; Haralur, G.; May, A. Effect of molecular weight on brittle-to-ductile transition temperature of polyetherimide. *J. Appl. Polym. Sci.* **2004**, *92*, 1666−1671.

(65) Kim, S.; Cotts, P. M.; Volksen, W. On-line measurement of the RMS radius of gyration and molecular weight of polyimide precursor fractions eluting from a size-exclusion chromatograph. *J. Polym. Sci., Part B: Polym. Phys.* **1992**, *30*, 177−183.

(66) Ciprari, D.; Jacob, K.; Tannenbaum, R. Characterization of Polymer Nanocomposite Interphase and Its Impact on Mechanical Properties. *Macromolecules* **2006**, *39*, 6565−6573.

(67) Zuo, P.; Jiang, J.; Chen, D.; Lin, J.; Zhao, Z.; Sun, B.; Zhuang, Q. Enhanced Interfacial and Dielectric Performance for Polyetherimide Nanocomposites through Tailoring Shell Polarities. *ACS Appl. Mater. Interfaces* **2023**, *15*, 23792−23803.

(68) Li, J.; Yin, J.; Liu, X.; Feng, Y.; Liu, Y.; Zhao, H.; Li, Y.; Zhu, C. Effect of structure on electric properties of Polyimide/Al2O3 composites investigated by SAXS. *2018 12th International Conference on the Properties and Applications of Dielectric Materials*, 2018.

(69) Holt, A. P.; Griffin, P. J.; Bocharova, V.; Agapov, A. L.; Imel, A. E.; Dadmun, M. D.; Sangoro, J. R.; Sokolov, A. P. Dynamics at the Polymer/Nanoparticle Interface in Poly(2-vinylpyridine)/Silica Nanocomposites. *Macromolecules* **2014**, *47*, 1837−1843.

(70) Seiler, J.; Kindersberger, J. Insight into the interphase in polymer nanocomposites. *IEEE Trans. Dielectr. Electr. Insul.* **2014**, *21*, 537−547.

(71) Ohrt, C.; Rätzke, K.; Oshima, N.; Kobayashi, Y.; O'Rourke, B. E.; Suzuki, R.; Uedono, A.; Faupel, F. Free Volume Profiles at Polymer-Solid Interfaces Probed by Focused Slow Positron Beam. *Macromolecules* **2015**, *48*, 1493−1498.

(72) Jean, Y. C.; Zhang, J.; Chen, H.; Li, Y.; Liu, G. Positron annihilation spectroscopy for surface and interface studies in nanoscale polymeric films. *Spectrochim. Acta, Part A* **2005**, *61*, 1683−1691.

(73) Jouault, N.; Moll, J. F.; Meng, D.; Windsor, K.; Ramcharan, S.; Kearney, C.; Kumar, S. K. Bound Polymer Layer in Nanocomposites. *ACS Macro Lett.* **2013**, *2*, 371−374.

(74) Popov, I.; Carroll, B.; Bocharova, V.; Genix, A.-C.; Cheng, S.; Khamzin, A.; Kisliuk, A.; Sokolov, A. P. Strong Reduction in Amplitude of the Interfacial Segmental Dynamics in Polymer Nanocomposites. *Macromolecules* **2020**, *53*, 4126−4135.

(75) Zhang, B.; Chen, X.; Lu, W.; Zhang, Q. M.; Bernholc, J. Morphology-induced dielectric enhancement in polymer nanocomposites. *Nanoscale* **2021**, *13*, 10933−10942.